PHOTONICS Research

Broadband supercontinuum generation in nitrogen-rich silicon nitride waveguides using a 300 mm industrial platform

Christian Lafforgue,[1,†,*] Sylvain Guerber,[1,2,†] Joan Manel Ramirez,[3] Guillaume Marcaud,[1] Carlos Alonso-Ramos,[1] Xavier Le Roux,[1] Delphine Marris-Morini,[1] Eric Cassan,[1] Charles Baudot,[2] Frédéric Boeuf,[2] Sébastien Cremer,[2] Stéphane Monfray,[2] and Laurent Vivien[1]

[1]Centre for Nanoscience and Nanotechnology (C2N), CNRS, Université Paris-Sud, Université Paris-Saclay, UMR 9001, 91405 Orsay Cedex, France
[2]Technologie R&D, STMicroelectronics, SAS, 850 rue Jean Monnet, 38920 Crolles, France
[3]III-V lab, a joint venture from Nokia Bell Labs, Thales and CEA, 1 Avenue Augustin Fresnel, 91767 Palaiseau Cedex, France
*Corresponding author: christian.lafforgue@c2n.upsaclay.fr

Received 2 October 2019; revised 30 December 2019; accepted 5 January 2020; posted 6 January 2020 (Doc. ID 379555); published 27 February 2020

We report supercontinuum generation in nitrogen-rich (N-rich) silicon nitride waveguides fabricated through back-end complementary-metal-oxide-semiconductor (CMOS)-compatible processes on a 300 mm platform. By pumping in the anomalous dispersion regime at a wavelength of 1200 nm, two-octave spanning spectra covering the visible and near-infrared ranges, including the O band, were obtained. Numerical calculations showed that the nonlinear index of N-rich silicon nitride is within the same order of magnitude as that of stoichiometric silicon nitride, despite the lower silicon content. N-rich silicon nitride then appears to be a promising candidate for nonlinear devices compatible with back-end CMOS processes.

https://doi.org/10.1364/PRJ.379555

1. INTRODUCTION

For many years, nonlinear optics has been unlocking new functionalities in optical communications (imaging or sensing, for example). Among these functionalities, we can cite electro-optic modulation through the Pockels effect, parametric amplification, or frequency conversion. There is a particular interest in applications involving frequency conversion. In this context, third-order nonlinear effects are of great concern, especially supercontinuum generation (SCG).

The latter has been widely studied in photonic crystal fibers [1], leading to advances in optical coherence tomography [2], precise measurement of optical frequencies [3], sensing and microscopy [4], to name a few. Recently, efforts have been made to develop SCG on-chip. High nonlinearities have been achieved, e.g., in chalcogenide glasses [5] or III–V materials [6,7]. However, these materials are not appropriate for large scale and low-cost production of compact electronics and photonics devices due to their lack of complementary-metal-oxide-semiconductor (CMOS) compatibility. This obstacle can obviously be overcome with silicon photonics. Silicon has a high nonlinear index, and interesting SCG results have been demonstrated in the past few years [8–14]. However, the large two-photon absorption (TPA) in the near-infrared wavelength range is a major drawback for nonlinear photonics using silicon [15]. On the other hand, a silicon nitride (SiN_x) platform is compatible with silicon technology and offers a nonlinear index 10 times higher than that of silicon dioxide with negligible TPA in the near-infrared wavelength range [16]. Hence, in the last decade, multiple studies have demonstrated wide SCG in SiN_x waveguides featuring broadband spectra [17–29]. Applications of supercontinuum in SiN_x have been shown with, for example, an f-to-2f interferometer for carrier envelope offset frequency detection [21,24,30–32], or mid-infrared generation of dispersive waves (DWs) for gas spectroscopy [28]. However, most of the reported SiN_x devices were fabricated using high temperature processes such as low-pressure chemical vapor deposition (LPCVD) or annealing steps to avoid cracks in the films and to achieve ultralow linear losses. Such high temperature fabrication steps are not compatible with back-end CMOS processes, hindering the integration of SiN_x active devices on electronic–photonic-integrated circuits for large-scale and low-cost production. Plasma-enhanced chemical vapor deposition (PECVD) addresses this issue since it is a low temperature deposition method (<500°C) widely used to deposit SiN_x films in CMOS foundries. Nonetheless, this deposition method involves the use of precursor gas such as silane, resulting in N–H dangling bonds in the SiN_x film, known to be responsible for

strong absorption at wavelengths around 1.5 μm. Recently, results have been published indicating the possibility of drastically reducing the linear losses at 1550 nm by employing deuterated SiN_x to shift the absorption band due to N–H bonds from 1.5 μm to 2 μm, allowing low loss in the C band without needing high temperature processes [33]. Wang *et al.* also established a back-end CMOS-compatible process to fabricate silicon-rich nitride waveguides [34] through bandgap engineering. Despite showing good nonlinear properties and low TPA at 1550 nm wavelength, the linear losses are still high (10 dB/cm) because of Si–H and N–H bonds as a result of the film deposition method. Other work has been done on an annealing-free process using stoichiometric SiN_x based on an ultralow deposition rate in LPCVD [35]. Several deposition steps with different orientation of the wafer are operated to avoid cracks by spreading the tensile stress in diverse directions. This study demonstrated a frequency comb generation by pumping a waveguide at 1550 nm wavelength. These methods can be back-end compatible solutions for nonlinear photonics in the C band, but still no advances have been shown to reduce linear losses in the O band (1260–1360 nm) with similar processes. In this work, we focus on SCG within this range in the frame of the STMicroelectronics industrial platform, aiming at data communications application at 1.31 μm wavelength. In this case, it is necessary to reduce the effective index of the SiN_x waveguide for optimal fiber-to-chip coupling. The use of a nitrogen-rich (N-rich) SiN_x is favorable in this case since the refractive index of SiN_x decreases when increasing the amount of nitrogen [36], and it can be deposited with a low-temperature PECVD technique. Moreover, the N–H bonds do not affect the propagation loss in the O band, and it even has been reported that linear losses at 1.31 μm are lower for N-rich SiN_x (<1 dB/cm) than for stoichiometric SiN_x [36]. This is the approach we chose in this study, as it permits us to obtain low linear-loss films through a simple back end of line-compatible process appropriate for the STMicroelectronics platform. Here we report a two-octave spanning SCG covering the visible range and the O band in N-rich SiN_x waveguides fabricated on a 300 mm platform at STMicroelectronics. Despite the nonlinear index of N-rich SiN_x being unknown, we estimated the nonlinear coefficient of our device by fitting curves obtained through numerical simulations to the experimental data. It appears that the nonlinear coefficient of our N-rich SiN_x waveguides is of the same order of magnitude as the one predicted for a stoichiometric Si_3N_4 waveguide with the same dimensions ($\gamma \simeq 1\ W^{-1} \cdot m^{-1}$). Since many SCG applications rely on coherence, we investigated the latter through numerical simulation by calculating the first-order degree of mutual coherence. It shows that for waveguides slightly longer than the soliton fission length, the supercontinuum spectrum exhibits a high coherence over more than one octave. Therefore, N-rich SiN_x waveguides appear to be a promising platform to develop large-scale nonlinear photonics.

2. SAMPLE FABRICATION

The waveguides were fabricated in STMicroelectronics facilities on a 300 mm platform. First, a thermal oxidation of a silicon substrate is performed to obtain a 600 nm-thick silicon dioxide (SiO_2) layer. Two tetraethyl orthosilicate (TEOS) deposition steps are carried out to form a total of 2 μm-thick SiO_2 layer. Then a 600 nm-thick N-rich SiN_x film is deposited with low-temperature PECVD (480°C, <5 Torr with SiH_4, NH_3, and N_2 gas). Finally, a deep-UV lithography step followed by an etching to define the waveguide was carried out. Since the nonlinear coefficient of N-rich SiN_x is unknown and expected to be lower than the nonlinear coefficient of stoichiometric SiN_x, we fabricated long waveguides to have an important nonlinear interaction length. Thus, the initial design consists in a spiral constituted of two different widths: a narrow-enough section to be single-mode in the bending regions to prevent important bending loss; and a larger multimode section to reduce the overlap between the fundamental mode and the sidewalls in order to diminish the linear propagation loss in the straight regions. We performed numerical simulations using a mode solver to find suitable waveguide widths for the single-mode and multimode regions for wavelengths lower than 1300 nm, since at higher wavelengths, the linear losses of N-rich SiN_x increase [36]. For a 700 nm width, the waveguide is single-mode in the near-infrared wavelength range (1000–1300 nm) while confining the light well. This value is then the one we used for the single-mode regions. For widths larger than 1000 nm, the waveguide is multimode in the near-infrared wavelength range. Furthermore, the multimode section is engineered to optimize the anomalous dispersion, as reported in the next section. Transverse-electric (TE) polarization will be used because the mode simulations show a lower modal effective area A_{eff} than the transverse-magnetic (TM) polarization ($A_{eff} = 0.58\ \mu m^2$ in TE, $A_{eff} = 0.72\ \mu m^2$ in TM for a 1200 nm-wide waveguide at 1200 nm wavelength), which is an advantage for SCG as it

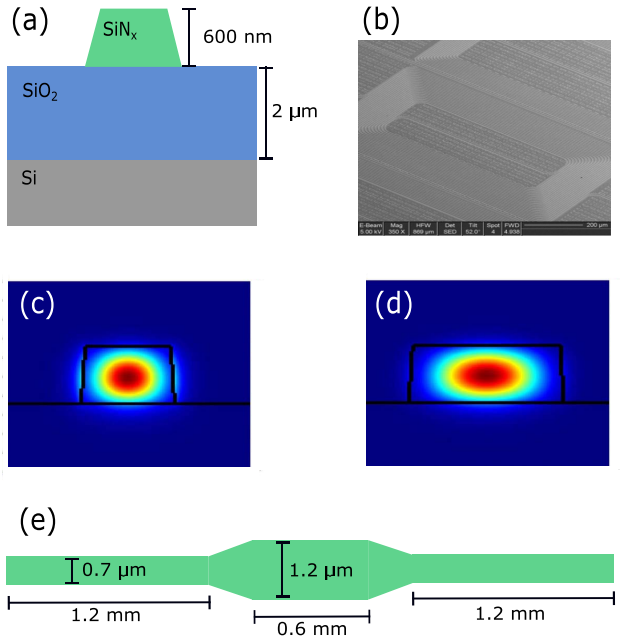

Fig. 1. (a) Schematic view of the waveguide section; (b) SEM view of spiral waveguide; (c) and (d) TE mode profile at 1200 nm wavelength for a 700 nm-wide waveguide and a 1200 nm-wide waveguide, respectively; (e) schematic view of the final design for the straight waveguide (top view).

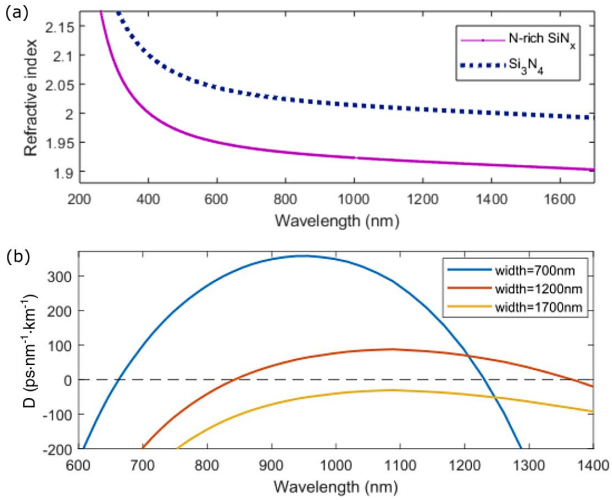

Fig. 2. (a) Refractive index of N-rich SiN_x measured by ellipsometry compared to Si_3N_4; (b) calculated dispersion parameter in an N-rich SiN_x waveguide for different widths.

results in a higher effective nonlinear coefficient. In addition to the spirals, straight waveguides were also fabricated. As discussed further in the paper, both waveguide sections present in the spirals affect the SCG. To be able to compare the results of the spirals to the shorter straight waveguides, the latter are also constituted of the two different waveguide sections, linked by a 200 μm-long taper providing an adiabatic transition. A schematic view of a waveguide cross section and a scanning electron microscope view of a fabricated spiral are represented in Figs. 1(a) and 1(b). The waveguide's sidewalls are tilted by 3° due to the etching process.

To characterize the index of the deposited film, an ellipsometry measurement was performed on an unpatterned N-rich SiN_x layer. The corresponding refractive index is plotted in Fig. 2(a). As expected, the refractive index of N-rich SiN_x is lower than the one of stoichiometric SiN_x (calculated using its Sellmeier equation from Ref. [37]), since the relative amount of silicon is reduced.

3. DISPERSION CALCULATIONS

Since pumping the nonlinear medium in the anomalous dispersion regime to achieve broadband SCG is required, we performed dispersion calculations to define the width of the multimode region. While the material dispersion of N-rich SiN_x is normal, it is possible to tailor the effective dispersion by playing on the dimensions of the waveguide geometry to obtain an anomalous dispersion for the guided mode. Numerical mode simulations were performed for several waveguide widths, and the dispersion parameter was then calculated, as shown in Fig. 2(b). Anomalous dispersion gets stronger when decreasing the width, as exhibited in the results for 700 and 1200 nm-wide waveguides. For the 1700 nm width, there is no anomalous dispersion regime, which is not convenient for SCG. It can be seen that for a 1200 nm-wide waveguide, a flat anomalous dispersion regime is obtained, covering the entire O band. The waveguides were then fabricated with a 1200 nm section for the multimode regions. It is important to notice that the 700 nm-wide section used for the single-mode regions also displays a strong anomalous dispersion regime that has to be taken into account in the analysis of the results. For the reference straight waveguides, a 1.2 mm-long section is 700 nm wide, and a taper adapts the width to a 0.6 mm-long 1200 nm-wide section. A second taper adapts the width back to 700 nm on a 1.2 mm length, as depicted in Fig. 1(e). Spirals with different lengths ranging from 0.6 to 5 cm were fabricated in order to characterize the propagation loss. After measuring the linear transmission of these spirals, we estimated the loss to be 0.6 dB/cm for the 700 nm width and 0.4 dB/cm for the 1200 nm width at 1300 nm wavelength.

4. EXPERIMENTAL RESULTS

The nonlinear characterization was performed on an 8.6 mm-long spiral waveguide and on a 3 mm-long straight waveguide using a 130 fs, 1 MHz pulsed laser with a tunable optical parametric amplifier to pump the device. The optical pulse is assumed to be a squared hyperbolic secant with a peak power coupled in the waveguide ranging from 250 W (37 pJ/pulse) to 9.5 kW (1.4 nJ/pulse). The pump wavelength was set to 1200 nm, near the maximum dispersion of the 1200 nm-wide section. The experimental setup is depicted in Fig. 3. Power is adjusted with a rotating half-wave plate followed by a polarization beam splitter. The TE mode is then injected into the sample through a wide taper with a 60× microscope objective. Output light is collected with a second 60× microscope objective before being reinjected into a fiber connected to the detectors. The coupling losses were estimated to be 7 ± 0.15 dB per facet, due to the diameter of the laser beam being larger than the input taper and due to reflection on the facets coming from the refractive index contrast between air and SiN_x. An optical spectrum analyzer collects wavelengths from 850 up to 1700 nm while a grating-based spectrometer collects visible and near-infrared light from 400 to 850 nm.

The experimental results are plotted in Fig. 4. For both waveguide types (spiral and straight), the experimental results were similar but the 3 mm-long waveguide has more power in the sides of the spectrum due to lower total propagation loss. In the following study, we focus on the 3 mm-long waveguide since the power is higher on the global spectrum in this configuration. For a peak power coupled in the waveguide lower than 1.5 kW, we observed a broadening from self-phase modulation (SPM) identifiable by the symmetric sidebands around the pump wavelength. For peak power higher than 1.5 kW, DWs appear, and a broadband supercontinuum is achieved with a −30 dB bandwidth starting at 400 nm and ending at 1600 nm, corresponding to a two-octave span [Fig. 4(d), black line]. There is a difference of background level for wavelength under 850 nm and over 850 nm because we used two different

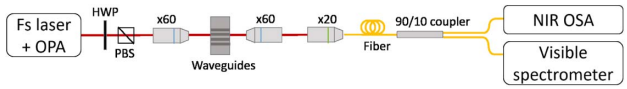

Fig. 3. Schematic view of the experimental setup. HWP, half-wave plate; PBS, polarization beam splitter; 60× and 20×, objectives.

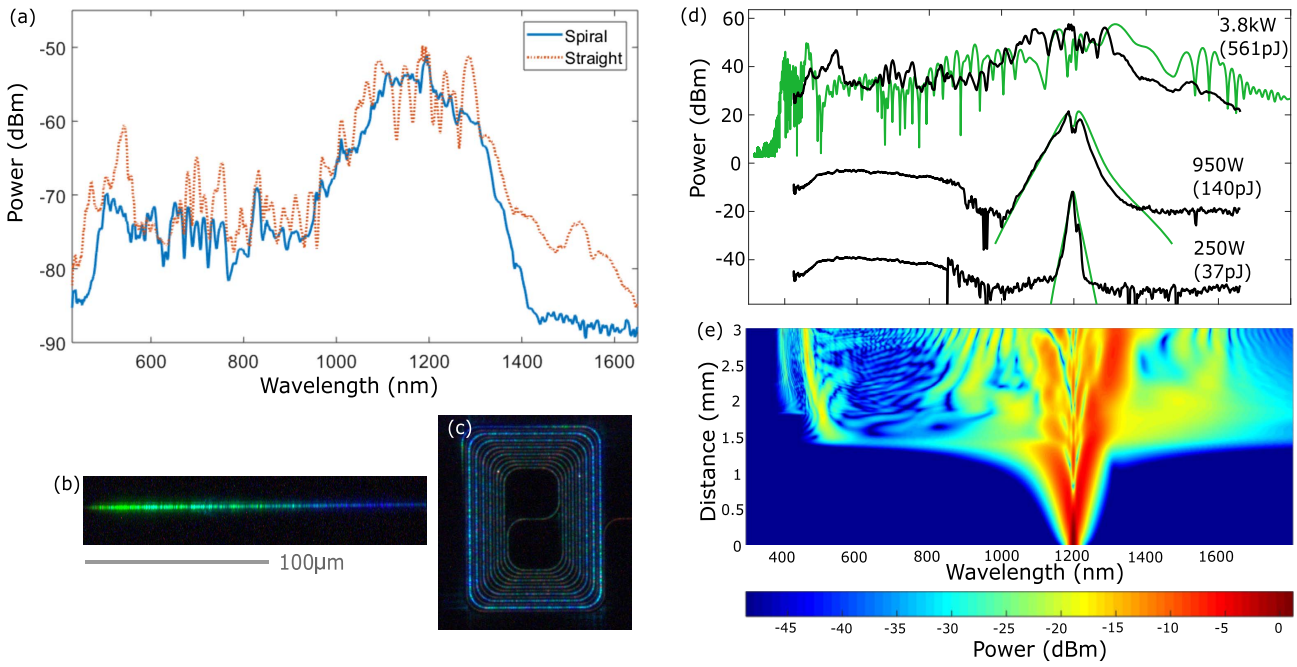

Fig. 4. (a) Experimental spectra for the 8.6 mm-long, 1200 nm-wide waveguide (blue dotted line) and the threefold 3 mm-long waveguide (black line) for an input peak power of 3.8 kW; (b) and (c) optical images of the 3 mm-long straight waveguide and the 8.6 mm-long spiral, respectively, from above, showing green and blue scattered light; (d) experimental (black lines) and simulated (green lines) spectra for different input peak powers; from bottom to top: 250 W, 950 W, 3.8 kW. Curves are arbitrarily shifted for better understanding. (e) Spectral evolution along the propagation direction for the simulated SCG 3.8 kW peak power.

detectors to extract the spectrum in these regions. A peak at 540 nm wavelength is attributed to a DW, since it is generated in the normal dispersion regime. In addition to the peak extracted from the spectrum, we noticed a green scattered light coming from the waveguide, which is in agreement with the peak measured at 540 nm, and also a blue scattered light as represented on the optical image of Figs. 4(b) and 4(c). This blue light is not seen on the measured spectrum due to the limited range of the visible spectrometer, whose lower boundary is 400 nm. This behavior is validated by numerical simulations, as discussed in the next section. De facto, we experimentally obtained a supercontinuum spanning over two octaves with a coupled pump power of 3.8 kW and an FWHM of 130 fs, corresponding to a coupled energy per pulse of 0.56 nJ, which is comparable to the results obtained in stoichiometric SiN_x reported in Refs. [18,21,25]. Still, this comparison does not permit us to draw any conclusion on the inherent material properties of the N-rich SiN_x, since the spectral broadening arises from a combination of material properties and waveguide dispersion.

5. NUMERICAL SIMULATIONS

To estimate the effective nonlinear coefficient of N-rich SiN_x, numerical simulations were performed to fit the experimental data, only relying on one fitting parameter, which is the nonlinear coefficient. The simulations consist in solving the generalized nonlinear Schrödinger equation (GNLSE) [38] using a fourth-order Runge–Kutta algorithm in the interaction picture method, as described in Ref. [39]. The GNLSE reads as follows:

$$\frac{\partial A}{\partial z} = -\frac{\alpha}{2} + i\sum_{k\geq 2}\beta_k \frac{i^k}{k!}\frac{\partial^k A}{\partial t^k} + i\gamma\left(1 + i\tau_{\text{shock}}\frac{\partial}{\partial t}\right)|A|^2 A, \quad \textbf{(1)}$$

where A denotes the temporal envelope of the pulse, z the distance along the propagation direction, α the linear propagation loss coefficient, β_k the k^{th} order of dispersion, t the time in the comoving frame at the phase velocity of the envelope, and τ_{shock} a time scale describing the self-steepening effect and first-order frequency dependence of the modal area [1]. Raman contribution was not included, as it is considered to be negligible in silicon nitride [32]. The nonlinear coefficient γ is related to the nonlinear index n_2 via the relation $\gamma = \omega_0 n_2(\omega_0)/[cA_{\text{eff}}(\omega_0)]$, with ω_0 being the center frequency of the pulse, c the light constant, and $A_{\text{eff}}(\omega_0)$ the effective modal area evaluated at ω_0. For the estimation of τ_{shock} and γ, the effective modal area A_{eff} was evaluated for each wavelength in the simulation window using a mode solver. Both waveguide widths of the threefold waveguide along the propagation direction are taken into account. We used the 250 and 950 W peak power experimental spectra as targets to fit the nonlinear parameter n_2, since for these powers we only observe SPM without soliton fission, enabling a more accurate estimation. When comparing the simulated spectra to the experimental spectra, we obtained a very good fitting of the curves at 250 and 950 W peak power for a nonlinear coefficient $n_2 \simeq 1.1 \times 10^{-19}$ $\text{m}^2 \cdot \text{W}^{-1}$, with an approximate uncertainty of 10% around this value (as outside this range there are either no noticeable SPM features or we observe a broadening that is too wide to be acceptable). This value corresponds to an effective nonlinear coefficient of

$\gamma \simeq 1.3\ \mathrm{W^{-1}\cdot m^{-1}}$ in the 700 nm-wide section and $\gamma \simeq 0.97\ \mathrm{W^{-1}\cdot m^{-1}}$ in the 1200 nm-wide section. At higher peak power, despite a good consistency of the curve shape, the simulated spectrum is higher than the experimental data for wavelengths above 1.4 μm [Fig. 4(d)]. This is attributed to a poor optical transmission at wavelengths higher than 1.4 μm due to a high concentration of N–H bonds and leakage through the substrate. The extracted value of the nonlinear coefficient n_2 is lower than the one of stoichiometric SiN_x ($n_2 = 2.4\times10^{-19}\ \mathrm{m^2\cdot W^{-1}}$ [16]) as expected with the reduction of silicon content; still, it is within the same order of magnitude.

It is also possible to predict theoretically the position of the DWs by solving the phase-matching condition [1],

$$\beta(\omega_{\mathrm{DW}}) - \beta(\omega_s) - \frac{\omega_{\mathrm{DW}} - \omega_s}{v_{g,s}} = \frac{\gamma P}{2}, \tag{2}$$

where $\beta(\omega)$ is the frequency-dependent dispersion, ω_{DW} is the frequency of the DW, ω_s is the center frequency of the most energetic soliton separating from the initial pulse, $v_{g,s}$ is the group velocity at the soliton frequency, and P is the peak power of the same soliton. The right side of Eq. (2) can be evaluated by calculating the order N of the initial pulse, as the peak power of the most energetic soliton is larger by a factor of $(2N-1)^2/N^2$ [40]. The left side of Eq. (2) is called integrated dispersion (β_{int}). With P_0 being the initial pulse peak power, Eq. (2) can then be written as

$$\beta_{\mathrm{int}} - \frac{(2N-1)^2}{N^2}\frac{\gamma P_0}{2} = 0. \tag{3}$$

The integrated dispersion is calculated by simulating the dispersion of the different waveguide sections. Figure 5 shows the calculated left side of Eq. (3) for the two different sections present in our waveguides (700 and 1200 nm widths), assuming ω_s and $v_{g,s}$ to be, respectively, the central pulsation and the group velocity of the injected pulse. The soliton order of the pulse is equal to 13 in the 700 nm-wide section and is equal to 12 in the 1200 nm-wide section. In total, the curves cross the zero axis 3 times, indicating that three DWs are phase-matched with the initial soliton: two associated with the 700 nm width at 390 and 1527 nm, and one associated with the 1200 nm width at 535 nm. The solution at 535 nm is in good agreement with the experimental data, and the third one at 1527 nm can be attributed to the bump observed in the experimental spectrum around 1530 nm. The third solution at 390 nm is not clearly visible in the measured spectrum since it is close to the limit of the spectrometer range, yet it is clearly visible in the simulated spectrum and is in good agreement with the dark blue scattered light from the sample, as shown in Figs. 4(b) and 4(c).

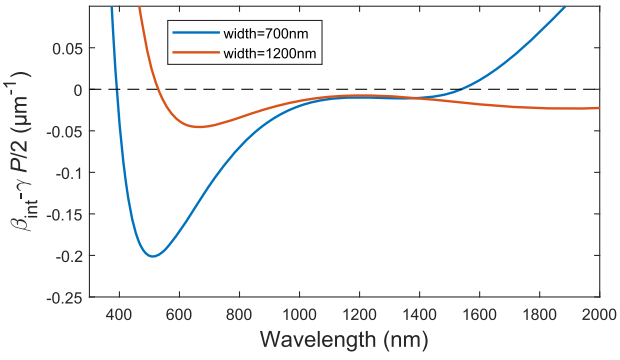

Fig. 5. Integrated dispersion for the two sections of the waveguide.

We also investigated numerically the supercontinuum coherence, as it is a key property in many SCG applications. The coherence simulations consist in a statistical calculation over a high number of simulated pairs of independent spectra seeded by a quantum shot noise. At each simulation, a shot noise is added to the initial field envelope, such as $A(t) = A_0(t) + a(t)$ with $A_0(t)$ the noiseless pulse, and $a(t)$ the shot noise. To implement the noise in the simulation, its intensity and phase were treated as Gaussian distributions whose variances are $\hbar\nu/(2\Delta t)$ and π, respectively, with Δt being the time discretization bin [41,42]. We simulated 40 individual spectra and the first-order degree of mutual coherence g_{12} was calculated according to the procedure described in Ref. [1], giving

$$|g_{12}(\omega)| = \frac{|\langle A_i^*(\omega)A_j(\omega)\rangle_{i\neq j}|}{\sqrt{\langle|A_i(\omega)|^2\rangle\langle|A_j(\omega)|^2\rangle}}, \tag{4}$$

where the angular bracket denotes an ensemble average over the pairs of simulated spectra $[A_i(\omega), A_j(\omega)]$. First, we performed the simulation for a 3 mm-long waveguide. The result is plotted in Fig. 6(b), where the orange line is the mutual degree of coherence, the blue lines are a superposition of the 40 simulated spectra, and the black line is the average spectrum. It appears that the output spectrum is submitted to strong intensity fluctuations and the degree of mutual coherence is weak. Such decoherence is typically due to modulation instability amplifying the noise intensity [1]. For better understanding, we plotted the first-order degree of coherence as a function of propagation

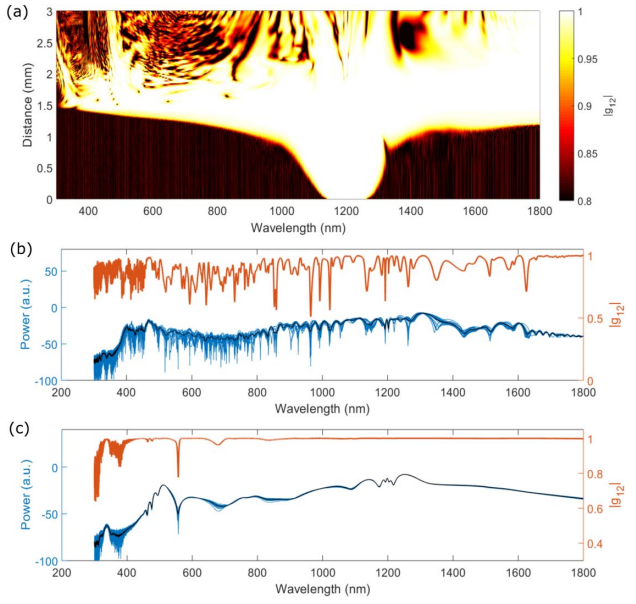

Fig. 6. (a) First-order degree of coherence plotted as a function of wavelength and propagation distance; (b) and (c) individual simulated spectra (blue lines), average of all the spectra (black line), and degree of mutual coherence (orange line) for a 3 mm-long and a 1.7 mm-long waveguide, respectively.

distance [Fig. 6(a)]. It can be seen that in the immediate vicinity of the SCG (at approximatively 1.5 mm distance), the spectrum is highly coherent all over its wavelength range. Then, the coherence is degraded. Hence, a solution to overcome the coherence degradation is to use shorter waveguides, with a length slightly higher than the soliton fission length, as shown in Ref. [19]. An example is shown in Fig. 6(c), where the spectrum and its coherence are plotted for a 1.7 mm-long waveguide. The very small intensity fluctuations indicate that the output spectrum is less sensitive to the noise, and the degree of mutual coherence is nearly unity in a wavelength range from 600 to 1800 nm. This can be useful for f-to-$2f$ interferometry applications, as the spectrum is highly coherent in a wavelength range covering more than one octave.

6. SUMMARY AND CONCLUSION

In summary, we demonstrated a new platform for back end-of-line photonics through the use of N-rich silicon nitride. Indeed, this platform allows the fabrication of low-loss devices with a low temperature process compatible with the cointegration of photonics systems with electronics and active components. The samples were fabricated on a 300 mm industrial platform, and the waveguides used in this study showed propagation losses lower than 1 dB/cm. Through dispersion engineering of a waveguide by playing on its dimensions, we showed that it is possible to obtain an anomalous dispersion regime, which then makes the waveguide suitable for SCG. Thus, we achieved the generation of an ultrabroadband supercontinuum covering two octaves, comprising the visible and near-infrared wavelength ranges. The 3 mm-long waveguide and the 8.6 mm-long spiral waveguide were pumped at 1200 nm with a 130 fs pulse with a coupled energy of 0.56 nJ. Numerical simulations permitted us to fit the experimental spectrum and to determine the nonlinear coefficient of the N-rich SiN_x used in the experiment. It resulted in an estimated $n_2 \simeq 1.1 \times 10^{-19}\ \mathrm{m}^2 \cdot \mathrm{W}^{-1}$, which is in the same order of magnitude as that of stoichiometric SiN_x. Additional simulations showed that it is possible to reach a very high coherence (>95%) over the whole spectrum for shorter waveguides (≃1.5 mm), which is a key property for many SCG applications. In conclusion, this novel material opens the way to integrated nonlinear photonics for telecommunications, spectroscopy, frequency metrology, or bioimaging, to name some examples.

Funding. European Research Council; Agence Nationale de la Recherche; Astre Essonne.

Disclosures. The authors declare no conflicts of interest.

†These authors contributed equally to this work.

REFERENCES

1. J. M. Dudley, G. Genty, and S. Coen, "Supercontinuum generation in photonic crystal fiber," Rev. Mod. Phys. **78**, 1135–1184 (2006).
2. L. Froehly and J. Meteau, "Supercontinuum sources in optical coherence tomography: a state of the art and the application to scan-free time domain correlation techniques and depth dependent dispersion compensation," Opt. Fiber Technol. **18**, 411–419 (2012).
3. T. Udem, R. Holzwarth, and T. Hänsch, "Optical frequency metrology," Nature **416**, 233–237 (2002).
4. C. Kaminski, R. Watt, A. Elder, J. Frank, and J. Hult, "Supercontinuum radiation for applications in chemical sensing and microscopy," Appl. Phys. B **92**, 367–378 (2008).
5. X. Gai, S. Madden, D.-Y. Choi, D. Bulla, and B. Luther-Davies, "Dispersion engineered $Ge_{11.5}As_{24}Se_{64.5}$ nanowires with a nonlinear parameter of 136 $W^{-1}m^{-1}$ at 1550 nm," Opt. Express **18**, 18866–18874 (2010).
6. J. J. Pigeon, S. Y. Tochitsky, C. Gong, and C. Joshi, "Supercontinuum generation from 2 to 20 μm in GaAs pumped by picosecond CO_2 laser pulses," Opt. Lett. **39**, 3246–3249 (2014).
7. J. Chiles, N. Nader, E. J. Stanton, D. Herman, G. Moody, J. Zhu, J. C. Skehan, B. Guha, A. Kowligy, J. T. Gopinath, K. Srinivasan, S. A. Diddams, I. Coddington, N. R. Newbury, J. M. Shainline, S. W. Nam, and R. P. Mirin, "Multifunctional integrated photonics in the mid-infrared with suspended AlGaAs on silicon," Optica **6**, 1246–1254 (2019).
8. N. Singh, M. Xin, D. Vermeulen, K. Shtyrkova, N. Li, P. T. Callahan, E. S. Magden, A. Ruocco, N. Fahrenkopf, C. Baiocco, N. Fahrenkopf, C. Baiocco, B. L. P.-P. Kuo, S. Radic, E. Ippen, F. X. Kärtner, and M. R. Watts, "Octave-spanning coherent supercontinuum generation in silicon on insulator from 1.06 μm to beyond 2.4 μm," Light Sci. Appl. **7**, 17131 (2018).
9. M. Sinobad, C. Monat, B. Luther-Davies, P. Ma, S. Madden, D. J. Moss, A. Mitchell, D. Allioux, R. Orobtchouk, S. Boutami, J.-M. Hartmann, J.-M. Fedeli, and C. Grillet, "Mid-infrared octave spanning supercontinuum generation to 8.5 μm in silicon-germanium waveguides," Optica **5**, 360–366 (2018).
10. B. Kuyken, T. Ideguchi, S. Holzner, M. Yan, T. W. Hänsch, J. Van Campenhout, P. Verheyen, S. Coen, F. Leo, and R. Baets, "An octave-spanning mid-infrared frequency comb generated in a silicon nanophotonic wire waveguide," Nat. Commun. **6**, 6310 (2015).
11. R. K. W. Lau, M. R. E. Lamont, A. G. Griffith, Y. Okawachi, M. Lipson, and A. L. Gaeta, "Octave-spanning mid-infrared supercontinuum generation in silicon nanowaveguides," Opt. Lett. **39**, 4518–4521 (2014).
12. N. Singh, D. D. Hudson, Y. Yu, C. Grillet, S. D. Jackson, A. Casas-Bedoya, A. Read, P. Atanackovic, S. G. Duvall, S. Palomba, B. Luther-Davies, S. Madden, D. J. Moss, and B. J. Eggleton, "Midinfrared supercontinuum generation from 2 to 6 μm in a silicon nanowire," Optica **2**, 797–802 (2015).
13. N. Nader, D. L. Maser, F. C. Cruz, A. Kowligy, H. Timmers, J. Chiles, C. Fredrick, D. A. Westly, S. W. Nam, R. P. Mirin, J. M. Shainline, and S. Diddams, "Versatile silicon-waveguide supercontinuum for coherent mid-infrared spectroscopy," APL Photon. **3**, 036102 (2018).
14. N. Nader, A. Kowligy, J. Chiles, E. J. Stanton, H. Timmers, A. J. Lind, F. C. Cruz, D. M. B. Lesko, K. A. Briggman, S. W. Nam, S. A. Diddams, and R. P. Mirin, "Infrared frequency comb generation and spectroscopy with suspended silicon nanophotonic waveguides," Optica **6**, 1269–1276 (2019).
15. L. Zhang, A. M. Agarwal, L. C. Kimerling, and J. Michel, "Nonlinear group IV photonics based on silicon and germanium: from near-infrared to mid-infrared," Nanophotonics **3**, 247–268 (2013).
16. K. Ikeda, R. E. Saperstein, N. Alic, and Y. Fainman, "Thermal and Kerr nonlinear properties of plasma-deposited silicon nitride/silicon dioxide waveguides," Opt. Express **16**, 12987–12994 (2008).
17. H. Zhao, B. Kuyken, S. Clemmen, F. Leo, A. Subramanian, A. Dhakal, P. Helin, S. Severi, E. Brainis, G. Roelkens, and R. Baets, "Visible-to-near-infrared octave spanning supercontinuum generation in a silicon nitride waveguide," Opt. Lett. **40**, 2177–2180 (2015).
18. M. A. G. Porcel, F. Schepers, J. P. Epping, T. Hellwig, M. Hoekman, R. G. Heideman, P. J. M. van der Slot, C. J. Lee, R. Schmidt, R. Bratschitsch, C. Fallnich, and K.-J. Boller, "Two-octave spanning supercontinuum generation in stoichiometric silicon nitride waveguides pumped at telecom wavelengths," Opt. Express **25**, 1542–1554 (2017).
19. A. R. Johnson, A. S. Mayer, A. Klenner, K. Luke, E. S. Lamb, M. R. E. Lamont, C. Joshi, Y. Okawachi, F. W. Wise, M. Lipson, U. Keller, and A. L. Gaeta, "Octave-spanning coherent supercontinuum generation in a silicon nitride waveguide," Opt. Lett. **40**, 5117–5120 (2015).
20. J. P. Epping, T. Hellwig, M. Hoekman, R. Mateman, A. Leinse, R. G. Heideman, A. van Rees, P. J. van der Slot, C. J. Lee, C. Fallnich, and

K.-J. Boller, "On-chip visible-to-infrared supercontinuum generation with more than 495 THz spectral bandwidth," Opt. Express **23**, 19596–19604 (2015).
21. D. R. Carlson, D. D. Hickstein, A. Lind, S. Droste, D. Westly, N. Nader, I. Coddington, N. R. Newbury, K. Srinivasan, S. A. Diddams, and S. B. Papp, "Self-referenced frequency combs using high-efficiency silicon-nitride waveguides," Opt. Lett. **42**, 2314–2317 (2017).
22. E. Baumann, E. V. Hoenig, E. F. Perez, G. M. Colacion, F. R. Giorgetta, K. C. Cossel, G. Ycas, D. R. Carlson, D. D. Hickstein, K. Srinivasan, S. B. Papp, N. R. Newbury, and I. Coddington, "Dual-comb spectroscopy with tailored spectral broadening in Si_3N_4 nanophotonics," Opt. Express **27**, 11869–11876 (2019).
23. A. J. Metcalf, T. Anderson, C. F. Bender, S. Blakeslee, W. Brand, D. R. Carlson, W. D. Cochran, S. A. Diddams, M. Endl, C. Fredrick, S. Halverson, D. D. Hickstein, F. Hearty, J. Jennings, S. Kanodia, K. F. Kaplan, E. Levi, E. Lubar, S. Mahadevan, A. Monson, J. P. Ninan, C. Nitroy, S. Osterman, S. B. Papp, F. Quinlan, L. Ramsey, P. Robertson, A. Roy, C. Schwab, S. Sigurdsson, K. Srinivasan, G. Stefansson, D. A. Sterner, R. Terrien, A. Wolszczan, J. T. Wright, and G. Ycas, "Stellar spectroscopy in the near-infrared with a laser frequency comb," Optica **6**, 233–239 (2019).
24. P. Manurkar, E. F. Perez, D. D. Hickstein, D. R. Carlson, J. Chiles, D. A. Westly, E. Baumann, S. A. Diddams, N. R. Newbury, and K. Srinivasan, "Fully self-referenced frequency comb consuming 5 watts of electrical power," OSA Continuum **1**, 274–282 (2018).
25. D. R. Carlson, D. D. Hickstein, A. Lind, J. B. Olson, R. W. Fox, R. C. Brown, A. D. Ludlow, Q. Li, D. Westly, H. Leopardi, T. M. Fortier, K. Srinivasan, S. A. Diddams, and S. B. Papp, "Photonic-chip supercontinuum with tailored spectra for counting optical frequencies," Phys. Rev. Appl. **8**, 014027 (2017).
26. A. S. Kowligy, D. D. Hickstein, A. Lind, D. R. Carlson, H. Timmers, N. Nader, D. L. Maser, D. Westly, K. Srinivasan, S. B. Papp, and S. A. Diddams, "Tunable mid-infrared generation via wide-band four-wave mixing in silicon nitride waveguides," Opt. Lett. **43**, 4220–4223 (2018).
27. D. Martyshkin, V. Fedorov, T. Kesterson, S. Vasilyev, H. Guo, J. Liu, W. Weng, K. Vodopyanov, T. J. Kippenberg, and S. Mirov, "Visible-near-middle infrared spanning supercontinuum generation in a silicon nitride (Si_3N_4) waveguide," Opt. Mater. Express **9**, 2553–2559 (2019).
28. D. Grassani, E. Tagkoudi, H. Guo, C. Herkommer, F. Yang, T. J. Kippenberg, and C.-S. Brès, "Mid infrared gas spectroscopy using efficient fiber laser driven photonic chip-based supercontinuum," Nat. Commun. **10**, 1553 (2019).
29. H. Guo, C. Herkommer, A. Billat, D. Grassani, C. Zhang, M. Pfeiffer, W. Weng, C.-S. Brès, and T. Kippenberg, "Mid-infrared frequency comb via coherent dispersive wave generation in silicon nitride nanophotonic waveguides," Nat. Photonics **12**, 330–335 (2018).
30. A. Mayer, A. Klenner, A. R. Johnson, K. Luke, M. Lamont, Y. Okawachi, M. Lipson, A. Gaeta, and U. Keller, "Frequency comb offset detection using supercontinuum generation in silicon nitride waveguides," Opt. Express **23**, 15440–15451 (2015).
31. Y. Okawachi, M. Yu, J. Cardenas, X. Ji, A. Klenner, M. Lipson, and A. L. Gaeta, "Carrier envelope offset detection via simultaneous supercontinuum and second-harmonic generation in a silicon nitride waveguide," Opt. Lett. **43**, 4627–4630 (2018).
32. A. Klenner, A. S. Mayer, A. R. Johnson, K. Luke, M. R. E. Lamont, Y. Okawachi, M. Lipson, A. L. Gaeta, and U. Keller, "Gigahertz frequency comb offset stabilization based on supercontinuum generation in silicon nitride waveguides," Opt. Express **24**, 11043–11053 (2016).
33. J. Chiles, N. Nader, D. D. Hickstein, S. P. Yu, T. C. Briles, D. Carlson, H. Jung, J. M. Shainline, S. Diddams, S. B. Papp, S. W. Nam, and R. P. Mirin, "Deuterated silicon nitride photonic devices for broadband optical frequency comb generation," Opt. Lett. **43**, 1527–1530 (2018).
34. T. Wang, D. K. T. Ng, S.-K. Ng, Y.-T. Toh, A. K. L. Chee, G. F. R. Chen, Q. Wang, and D. T. H. Tan, "Supercontinuum generation in bandgap engineered, back-end CMOS compatible silicon rich nitride waveguides," Laser Photon. Rev. **9**, 498–506 (2015).
35. H. El Dirani, A. Kamel, M. Casale, S. Kerdiles, C. Monat, X. Letartre, M. Pu, L. K. Oxenløwe, K. Yvind, and C. Sciancalepore, "Annealing-free Si_3N_4 frequency combs for monolithic integration with Si photonics," Appl. Phys. Lett. **113**, 081102 (2018).
36. T. D. Bucio, A. Z. Khokhar, C. Lacava, S. Stankovic, G. Z. Mashanovich, P. Petropoulos, and F. Y. Gardes, "Material and optical properties of low-temperature NH_3-free PECVD SiN x layers for photonic applications," J. Phys. D **50**, 025106 (2016).
37. K. Luke, Y. Okawachi, M. R. E. Lamont, A. L. Gaeta, and M. Lipson, "Broadband mid-infrared frequency comb generation in a Si_3N_4 microresonator," Opt. Lett. **40**, 4823–4826 (2015).
38. Q. Lin, O. J. Painter, and G. P. Agrawal, "Nonlinear optical phenomena in silicon waveguides: modeling and applications," Opt. Express **15**, 16604–16644 (2007).
39. J. Hult, "A fourth-order Runge-Kutta in the interaction picture method for simulating supercontinuum generation in optical fibers," J. Lightwave Technol. **25**, 3770–3775 (2007).
40. S. Roy, S. K. Bhadra, and G. P. Agrawal, "Effects of higher-order dispersion on resonant dispersive waves emitted by solitons," Opt. Lett. **34**, 2072–2074 (2009).
41. R. Paschotta, "Noise of mode-locked lasers (part I): numerical model," Appl. Phys. B **79**, 153–162 (2004).
42. A. Ruehl, M. J. Martin, K. C. Cossel, L. Chen, H. McKay, B. Thomas, C. Benko, L. Dong, J. M. Dudley, and M. E. Fermann, "Ultrabroadband coherent supercontinuum frequency comb," Phys. Rev. A **84**, 011806 (2011).